

Entropy as a Gene-Like Performance Indicator Promoting Thermoelectric Materials

Ruiheng Liu, Hongyi Chen, Kunpeng Zhao, Yuting Qin, Binbin Jiang, Tiansong Zhang, Gang Sha, Xun Shi,* Ctirad Uher, Wenqing Zhang,* and Lidong Chen*

High-throughput explorations of novel thermoelectric materials based on the Materials Genome Initiative paradigm only focus on digging into the structure-property space using nonglobal indicators to design materials with tunable electrical and thermal transport properties. As the genomic units, following the biogene tradition, such indicators include localized crystal structural blocks in real space or band degeneracy at certain points in reciprocal space. However, this nonglobal approach does not consider how real materials differentiate from others. Here, this study successfully develops a strategy of using entropy as the global gene-like performance indicator that shows how multicomponent thermoelectric materials with high entropy can be designed via a high-throughput screening method. Optimizing entropy works as an effective guide to greatly improve the thermoelectric performance through either a significantly depressed lattice thermal conductivity down to its theoretical minimum value and/or via enhancing the crystal structure symmetry to yield large Seebeck coefficients. The entropy engineering using multicomponent crystal structures or other possible techniques provides a new avenue for an improvement of the thermoelectric performance beyond the current methods and approaches.

In response to the global energy crisis and the debilitating impact of fossil fuels on the environment, thermoelectric (TE) materials have attracted worldwide attention for their ability to collect and convert industrial waste heat into useful electricity. A criterion for what constitutes a high performing TE material is the dimensionless TE figure of merit zT , defined as $zT = \alpha^2 \sigma T / \kappa$, where α is the Seebeck coefficient, σ is the

electrical conductivity, κ is the thermal conductivity, and T is the absolute temperature. Strong correlations among the above transport parameters limit the materials base of thermoelectricity to a few classic TE materials, and the zT values have remained limited to a range of 1–2 in the past decades.^[1–3] To meet the endlessly growing demands, the Materials Genome Initiative has been used for the fast design and screening of new thermoelectric materials by tailoring the real-space (R-space) structural building blocks or band degeneracy at certain reciprocal-space (K-space) points as a genome-like performance indicator based on first principles calculations.^[4,5]

In thermodynamics, entropy (S) measures the large number of microscopic configurations of a given material's macrostate from a global point of view. The entropy in a material can be enhanced through introducing element doping and alloying^[2] various atomic vibration states,^[3,6] liquid-like ionic migrations,^[7] or hierarchical structures.^[8] Maximizing the entropy in a material makes a significant impact on the material's microstructure and macroscopic properties clearly beyond doping or band engineering within limited R- or K-space, which is especially useful for thermoelectrics requiring the optimization of multiple interrelated physical quantities at one given material

Dr. R. Liu, H. Chen, K. Zhao, Dr. Y. Qin, B. Jiang, T. Zhang, Prof. X. Shi, Prof. W. Zhang, Prof. L. Chen
State Key Laboratory of High Performance Ceramics
and Superfine Microstructure
Shanghai Institute of Ceramics
Chinese Academy of Science
Shanghai 200050, China
E-mail: xshi@mail.sic.ac.cn; zhangwq@sustc.edu.cn; cld@mail.sic.ac.cn
H. Chen, K. Zhao, Dr. Y. Qin, B. Jiang
Shanghai Institute of Ceramics
University of Chinese Academy of Sciences
Beijing 100049, China
H. Chen
School of Physical Science and Technology
Shanghai Tech University
Shanghai 201210, China

Prof. G. Sha
School of Materials Science and Engineering
Nanjing University of Science and Technology
Nanjing 210094, China
Prof. C. Uher
Department of Physics
University of Michigan
Ann Arbor, MI 48109, USA
Prof. W. Zhang
Department of Physics
Southern University of Science and Technology
Shenzhen, Guangdong 518055, China

DOI: 10.1002/adma.201702712

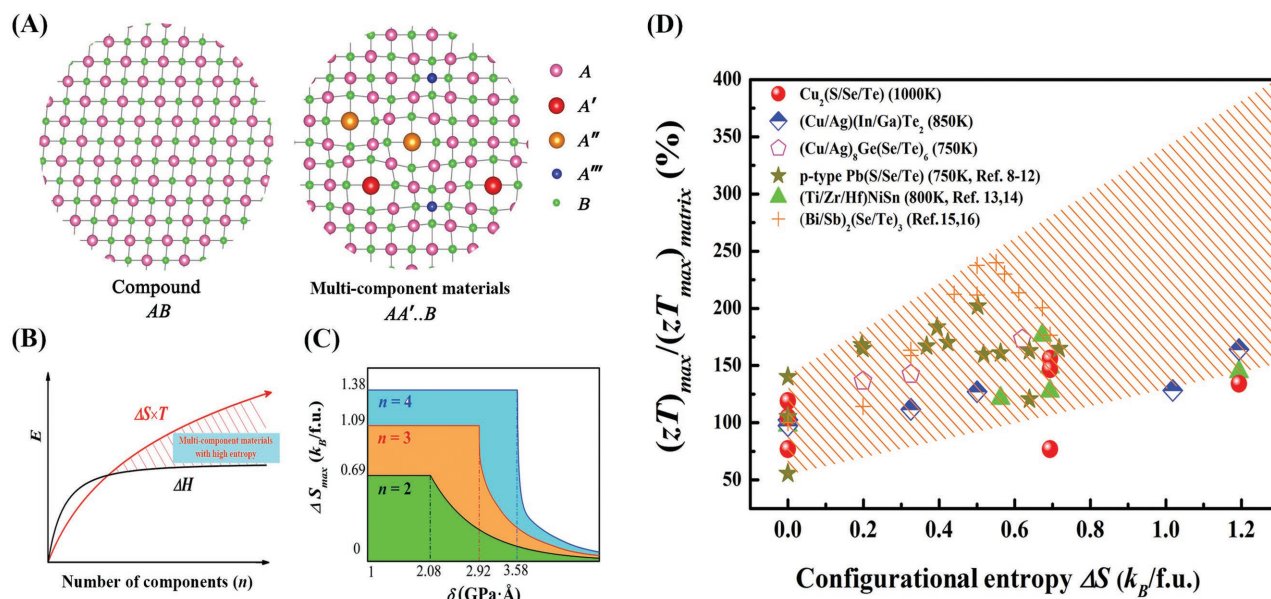


Figure 1. Enhanced TE properties through entropy engineering. A) Schematic diagram of the lattice framework in multicomponent materials compared to an ordinary binary compound. B) Schematic diagram of the entropy engineering with multicomponent TE materials. The red line and black line represent energies contributed by the configurational entropy (ΔS) and by the formation enthalpy (ΔH), respectively. C) The maximum configurational entropy (in units of k_B per formula unit) as a function of a material's solubility parameter δ for given multicomponent TE materials, where n is the number of components. D) Maximum TE Figure of merit (zT) as a function of the configurational entropy in $\text{Cu}_2(\text{S/Se/Te})$ -, $(\text{Cu/Ag})(\text{In/Ga})\text{Te}_2$ -, and $\text{Cu}_8\text{Ge}(\text{Se/Te})_6$ -based multicomponent TE materials. The zT s of $\text{Pb}(\text{S/Se/Te})$ - and $(\text{Ti/Zr/Hf})\text{NiSn}$ -based materials are taken from refs. [8–16].

state. Entropy indeed acts as an overall performance indicator to evaluate TE properties, just like a virtual but unique “gene” beyond localized crystal structural blocks in R-space or band degeneracy at certain K-space points. A particular example is using multicomponent alloying that specially alters configurational entropy, as shown in Figure 1A,B. Compared with simple compounds characterized by single-component atoms located at respective atomic positions, multicomponent materials have several structural components located at the same atomic sites, and thus have highly tunable entropy capable of strongly scattering lattice phonons and potentially enhancing the crystal structure symmetry to yield good electronic properties. However, there is currently no effective criterion to predict and screen high performance multicomponent TE materials due to the complexity of the crystal structure and chemical bonds in such materials. Since the solvent atoms are usually homogeneously distributed in materials, attempts to form a multicomponent structure, i.e., a solid solution with multiple components, result in a material that has similar chemical bonds as the matrix material. This fact prompted us to develop an elastic model to study the stability of multicomponent TE materials. We found that the maximum entropy for given multicomponent materials depends on the overall material's solubility parameter δ that is associated with the material's shear modulus, lattice constants, and mismatch in the atomic radius (see below). For a multicomponent material with given δ value, it is very easy to find the maximum entropy based on Figure 1C. Then, the high-throughput calculation for multicomponent TE materials with the desired entropy is performed, and several candidate materials with the zT values significantly higher than in the matrix are identified

(see Figure 1D). As an example, the maximum zT is up to 1.6 and 2.23 in $(\text{Cu/Ag})(\text{In/Ga})\text{Te}_2$ - and $\text{Cu}_2(\text{S/Se/Te})$ -based multicomponent TE materials, respectively (see the Supporting Information).

In multicomponent materials (see Figure 1A), the substituted atoms (A' , A'' ...) in equivalent lattice sites definitely change the material's total free energy, although they have similar chemical bonds and atomic coordination as the framework atom A. Because the substituted atoms (A' , A'' ...) have different atomic size and electronegativity compared to the matrix element (A), the enthalpy change (ΔH_{total}) is simply considered as a combination of the internal strain energy (ΔH_S) due to atomic size mismatch and fluctuations of the internal ionic field energy (ΔH_C) arising from the electron cloud redistribution according to the Hume–Rothery rules.^[17] In addition, the total energy is lowered by the entropy caused by multiple components located at the same atomic sites. Formally, the total free energy change (ΔE) is given by $\Delta E = \Delta H_S + \Delta H_C - \Delta S \times T$. Following Boltzmann's hypothesis, the configurational entropy (ΔS) is given by^[18]

$$\Delta S = k_B \ln \Omega = -N_A k_B \sum_{i=1}^n x_i \ln x_i, \quad \sum_{i=1}^n x_i = 1 \quad (1)$$

where k_B is the Boltzmann constant, Ω is the number of atomic occupation probability, n is the number of the substituted components, x_i is the mole content of the i th component, and N_A is Avogadro's number. In semiconductors, the magnitude of ΔH_C is very small (at the level of 0.01–0.1 $k_B T/f.u.$ at 300 K, see Table S1 in the Supporting Information) and thus can be ignored. Therefore, the change in enthalpy is dominated by the internal strain energy (ΔH_S) that is determined by the

average shear modulus and the mismatch in the unit cell (see Equation (S7) in the Supporting Information).

For a two-component TE semiconducting solid solution $(1-x)AB + xA'B \rightarrow A_{1-x}A'_x B$, the calculated change in enthalpy and atomic solubility reasonably agree with the *ab initio* calculations and experimental observations (see in Figure S1 in the Supporting Information and Figure 2A). We then define a parameter $\delta = \bar{G} \bar{R}^* (\Delta R^*)^2 / Z$ with units of $\text{GPa} \text{Å}^3$ as a criterion for judging the atomic solubility. Here \bar{G} is the average shear modulus, R^* is the effective lattice constant (defined by $R^* = \sqrt{\frac{a^2 + b^2 + c^2}{3}}$ for an orthorhombic structure and $\sqrt{\frac{(2a)^2 + c^2}{3}}$ for a hexagonal structure, where a , b , and c are the parameters of a unit cell, or the parameters of a supercell that is built close to a sphere), \bar{R}^* is the average effective lattice constant and ΔR^* is the difference in the effective lattice constant between AB and $A'B$ ($\Delta R^* = |R^*_{AB} - R^*_{A'B}|$), and Z is the

number of formula units in one unit cell or the corresponding supercell. For example, a supercell with lattice parameters of $(4a^* \times 4b^* \times c^*)$ is required to run such calculations for hexagonal Bi_2Te_3 -based materials, where a^* , b^* , and c^* are the lattice parameters of a conventional unit cell. With the above definitions, a low δ value means a low internal strain energy and high atomic solubility, and vice versa. As shown in Figure 2A, two-component solutions with δ below $2.08 \text{ GPa} \text{Å}^3$ can form complete solid solutions, such as $(\text{Cd}/\text{Hg})\text{Te}$, $\text{Pb}(\text{S}/\text{Se})$, $(\text{Rh}/\text{Ir})\text{Sb}_3$, $\text{Cu}_2(\text{S}/\text{Se})$, $\text{Cu}_2(\text{Se}/\text{Te})$, $(\text{Bi}/\text{Sb})_2\text{Te}_3$, $(\text{Cu}/\text{Ag})\text{InTe}_2$, and $(\text{Cu}/\text{Ag})\text{GaTe}_2$, while systems with δ larger than $2.08 \text{ GPa} \text{Å}^3$ can only result in partial solid solutions, such as $(\text{Co}/\text{Ir})\text{Sb}_3$, $(\text{Co}/\text{Rh})\text{Sb}_3$, $\text{Bi}_2(\text{Se}/\text{Te})_3$, and $\text{Pb}(\text{Se}/\text{Te})$. The systems with very large δ values, such as $\text{Pb}(\text{S}/\text{Te})$, have very low atomic solubility.

Ternary or multicomponent solid solution systems can be regarded as being derived from a quasibinary reaction of the type $(1-x)A_1 - yA''_y B + xA'_1 - yA''_y B \rightarrow (A_1 - xA'_x)_1 - yA''_y B$, where $A_1 - yA''_y B$, $A'_1 - yA''_y B$ are the quasimatrixes dissolving a third component $A''B$ with an initial content y . Our calculations show that the component $A''B$ actually relaxes the crystal lattice by reducing the internal strain energy by the magnitude of the suppressed strain energy determined mainly by y under a relation $(1-y)^{3.5}$ (see Equation (S11) in the Supporting Information). By accumulating all the reactions of binary solid solutions and subreactions of quasibinary solutions, the total free energy change in an equimolar multicomponent solution is

$$\Delta E = MN_A \cdot \bar{\delta} \cdot \left[\sum_{i=2}^n \left(1 - \frac{1}{i} \right) \frac{1}{i} \cdot \left(\frac{i}{n} \right)^{3.5} \right] - N_A k_B T \ln(n) \quad (2)$$

where $\bar{\delta}$ is the average δ value of all separate binary solutions and M is a dimensionless constant with an approximate value of 7.34 in semiconductors. The first term in Equation (2) represents the change in enthalpy, referred to the internal strain energy, and the second term represents the energy from the configurational entropy. Figure 2B shows the energy variation when increasing the number of substituted components. Due to the rapidly increasing configurational entropy, a complete solid solution is obtained when the number of substituted components is large enough, regardless of the intrinsic nature of the components. This is similar to cases of high entropy-stabilized alloys and oxides in which five or more substituted components with far different atomic sizes and electronegativities leads to a single *bcc* or *fcc* phase.^[19,20] However, the number of substituted components in TE semiconductors usually does not exceed 4 or 5. Therefore, in order to form a complete solid solution, the parameter $\bar{\delta}$ should be less than 2.92, 3.58, and $4.12 \text{ GPa} \text{Å}^3$ for the multicomponent materials with 3, 4, and 5 components, respectively.

Our model shown above provides a direct criterion by which to screen and identify candidate multicomponent TE materials with high configurational entropy. The current elastic model works well for materials with identical crystal structures; thus, high-throughput selection can be performed based on the experimental lattice parameters or atomic sizes, and the materials' shear moduli. We looked at various typical TE materials with cubic or cubic-like structures, the physical properties of which are listed in Tables S2 and S4 (Supporting Information). Our calculations show that $(\text{Ti}/\text{Zr}/\text{Hf})\text{NiSn}$ and $(\text{Ti}/\text{Zr}/\text{Hf})\text{CoSb}$

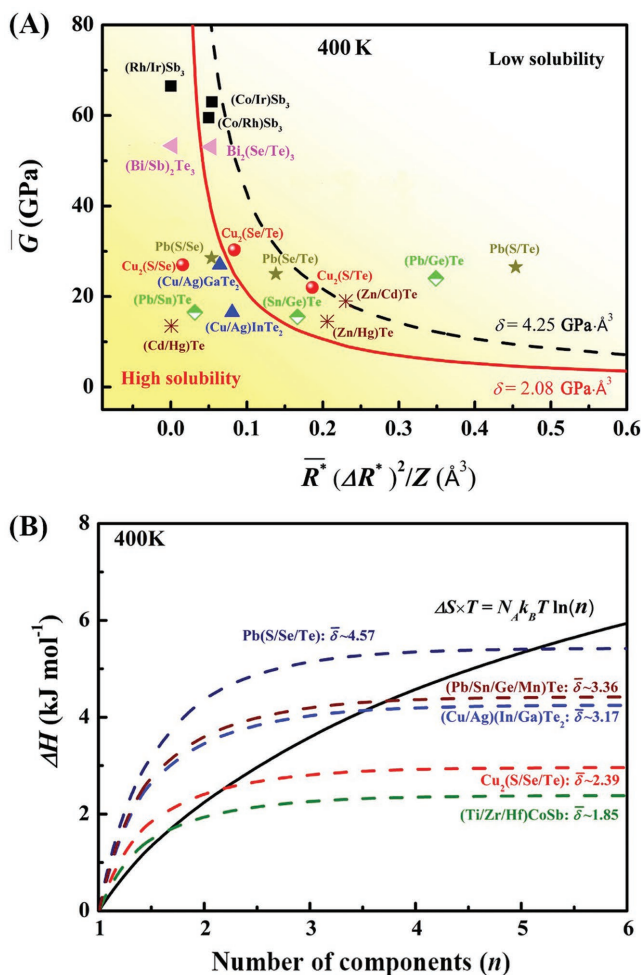


Figure 2. Energies in multicomponent TE materials. A) Average shear modulus (\bar{G}) as a function of $\bar{R}^* (\Delta R^*)^2 / Z$ in two-component solutions. The red and black lines represent the curves with the solubility of 0.5 and 0.01, respectively. B) Internal strain energy as a function of the number of components (n). The black solid line represents the energy contributed by configurational entropy. The dashed lines illustrate the relation in particularly useful TE materials.

can form equimolar ternary solid solutions, which is reasonably consistent with the experiments.^[21] Furthermore, our model shows that $\text{Cu}_2(\text{S/Se/Te})$ can form equimolar ternary solid solutions, while $(\text{Cu/Ag})(\text{In/Ga})\text{Te}_2$ and $(\text{Mn/Ge/Sn/Pb})\text{Te}$ can be realized as equimolar quaternary solutions. In contrast, $\text{Pb}(\text{S/Se/Te})$ has a too large value of δ to form equimolar ternary solid solutions.

Aiming to form solid solutions and test our predictions experimentally, we selected and synthesized several candidate multicomponent TE materials, e.g., $(\text{Cu/Ag})(\text{In/Ga})\text{Te}_2$, $\text{Cu}_2(\text{S/Se/Te})$, and $(\text{Mn/Ge/Sn/Pb})\text{Te}$ -based materials. X-ray diffraction analysis shows all these materials to be phase pure without any obvious impurity phases (see Figures S3–S5, Supporting Information). Electron probe microanalysis reveals that all elements are homogeneously distributed throughout the entire sample without any obvious agglomeration of elements (see the Supporting Information). Furthermore, we have performed a 3D-atom probe tomography analysis to check the distribution of elements on the atomic-scale. Taking $\text{Cu}_2(\text{S/Se/Te})$ -based multicomponent materials as an example,

the ionic mass spectrum of $\text{Cu}_2\text{S}_{1/3}\text{Se}_{1/3}\text{Te}_{1/3}$ is shown in Figure 3A. The reconstructed 3D atomic maps based on the ionic mass spectrum are shown in Figure 3B. No aggregation of chalcogen atoms is observed. This is further confirmed by the analysis of the nearest-neighbor (NN) atomic distributions, as shown in Figure 3C. The measured NN atomic distance histograms of each element are completely overlapped with the calculated curves (black curve in Figure 3C) based on the assumption that all elements are randomly distributed in the sample. All these results unequivocally demonstrate that all components are extremely homogeneous on the macroscale, the nanoscale, and even on the atomic-scale. This is consistent with our calculations because these multicomponent TE materials are phase-pure and thermodynamically stable.

Beyond the high-throughput screening and identification of candidate multicomponent TE materials, TE properties are also significantly optimized and improved by increasing the material's entropy because it is a gene-like performance indicator. Increasing entropy in a TE material definitely leads to a greater number of microscopic configurations that may significantly

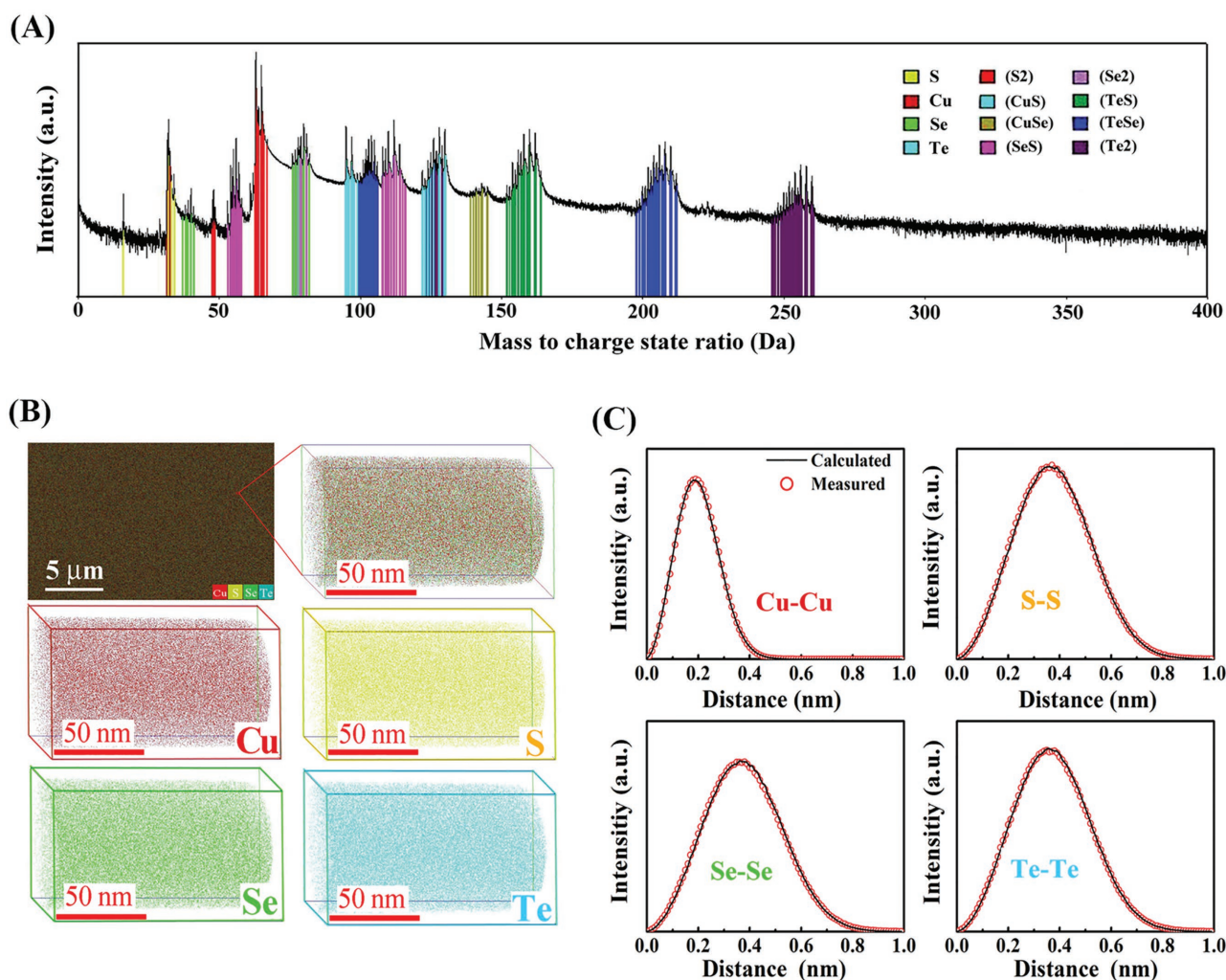


Figure 3. 3D-Atomic Probe Tomography detection for $\text{Cu}_2\text{S}_{1/3}\text{Se}_{1/3}\text{Te}_{1/3}$. A) Ionic mass spectrum, B) 3D-atomic maps, and C) nearest-neighbor atomic distribution histograms of the four elements. The black lines represent the calculated curves assuming all elements are homogeneously and randomly distributed in the material.

introduce extra phonon disorder and open a new window to tune electrons, and thus affect both electrical and thermal transports. First is a significantly decreased lattice thermal conductivity. Such a large number of microscopic configurations in the materials with high entropy implies the existence of numerous lattice defects that provide extra phonon point defect scattering to suppress heat conduction. Especially for the multicomponent materials shown above, there exist strong mass and strain fluctuations among the various components that significantly depress the material's lattice thermal conductivity.^[22] With the continuous enhancement of entropy by increasing the solute components, the phonon disorder is incessantly increased and finally may reach a critical state like a glass. Correspondingly, the lattice thermal conductivity is depressed down to the glass limit in a solid, i.e., the minimum lattice thermal conductivity. This is illustrated in Figure 4A. When the number of solid solution components increases, a huge suppression in the lattice

thermal conductivity is observed, with the value approaching the minimum thermal conductivity^[6] (κ_{\min}) in solids. The required number of components to reach κ_{\min} varies for different materials. For the systems with high initial thermal conductivity, such as half-Heusler alloys,^[22] skutterudites,^[23] and chalcopyrites,^[24] the required number of substituted components to reach κ_{\min} at 300 K is at least 5 or 6. For example, the room temperature κ_L of around 6–9 W m⁻¹ K⁻¹ in the matrix of CuInTe₂ or CuGaTe₂ is reduced to 2–4 W m⁻¹ K⁻¹ for the two-component materials with an entropy of 0.69 k_B /f.u., and down to 1.4 W m⁻¹ K⁻¹ for the four-component materials with an entropy of 1.38 k_B /f.u. in this study. For matrix compounds with a moderate initial κ_L , such as (Ca/Yb)Zn₂Sb₂,^[25] Mg₂(Si/Ge/Sn),^[26–28] Bi₂(S/Se/Te)₃,^[29] and Pb(S/Se/Te),^[9–11] 3 or 4 different kinds of substituted components are required to reach κ_{\min} . For example, the room temperature κ_L of around 2.5 W m⁻¹ K⁻¹ in the PbTe matrix^[9] is reduced to 1.0 W m⁻¹ K⁻¹ (just a little higher than the κ_{\min} in PbTe) for three-component materials with an entropy of 0.7 k_B /f.u.^[11] For matrix materials having an extremely low κ_L , such as liquid-like materials Cu₂(S/Se/Te) and (Cu/Ag)₈Ge(Se/Te)₆, the κ_L values are already nearly equal to the κ_{\min} , and these values are maintained in essentially all multicomponent materials.

The second effect concerns the increasing configurational entropy that may enhance the crystal structure symmetry and thus improve electronic transport properties, especially for matrix materials having low symmetry structures. When the configurational entropy increases, environmental heat activations and fluctuations lead to more disordered and homogenous atomic distributions throughout the crystal lattice in materials possessing multicomponent-occupied identical atomic sites. This may increase the material's crystal symmetry. When the entropy is high enough, all multicomponent materials tend to possess a high symmetry cubic structure. When the entropy is not so high, the symmetry of the structure may still be improved or any structural transition temperature may be reduced. This has been shown in many experiments,^[30,31] and is confirmed here by our studies. For example, single Cu₂X (X = Te, Se, or S) compounds generally crystallize with the monoclinic structure at room temperature ($P2_1/c$ for Cu₂S^[32] and $C2/c$ for Cu₂Se),^[33] but the symmetry is increased to hexagonal in Cu₂S_{0.5}Te_{0.5}, Cu₂S_{0.5}Se_{0.5}, and Cu₂S_{1/3}Se_{1/3}Te_{1/3} when the configuration entropy is above 0.6 k_B /f.u. (see Figure S3, Supporting Information). This promotion of the crystal symmetry in multicomponent TE materials definitely changes their electronic band structure. High symmetry crystal structures tend to form multiband electronic bands or overlapped bands near the Fermi level due to the high symmetry inducing more equivalent positions in both real and reciprocal space. This can significantly increase the electronic density-of-states and effective mass, and thus enhance the Seebeck coefficient. For the systems with initially high crystal symmetry, such as (Cu/Ag)(In/Ga)Te₂, there is no obvious trend in the variation of the Seebeck coefficient because there is either no structural variation or the structural variation is very weak (see Figure 4B). However, for the systems with initially low crystal symmetry, the Seebeck coefficient of multicomponent TE materials is obviously superior to the matrix compounds. Taking Cu₂(S/Se/Te) as an example, when the carrier concentration is in the range from 1.0×10^{21}

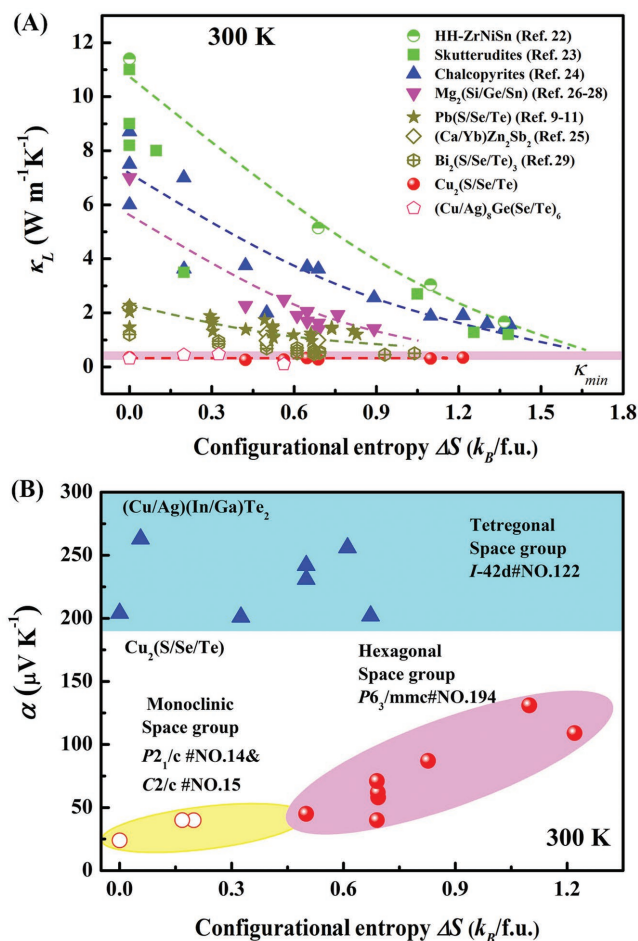


Figure 4. Lowered lattice thermal conductivity (κ_L) and improved Seebeck coefficient (α) in multicomponent TE materials. A) κ_L as a function of the configurational entropy. The red zone presents the κ_{\min} , and the dashed lines are guides to the eyes. B) Room temperature α as a function of the configurational entropy in (Cu/Ag)(In/Ga)Te₂- and Cu₂(S/Se/Te)-based multicomponent materials with respective carrier concentrations in the range of $(1.0\text{--}2.0) \times 10^{19}$ and $(1.0\text{--}3.0) \times 10^{21}$ cm⁻³. The data for (Cu/Ag)(In/Ga)Te₂- and Cu₂(S/Se/Te)-based materials are listed in Table S3, Supporting Information.

to $3.0 \times 10^{21} \text{ cm}^{-3}$, the Seebeck coefficient at 300 K is merely 20–40 $\mu\text{V K}^{-1}$ in the monoclinic structure, but it significantly improves to 70–130 $\mu\text{V K}^{-1}$ in the hexagonal structure having large entropy (see Figure 4B). Specifically, the carrier concentrations of the matrix compound Cu_{2-x}Se ($1.51 \times 10^{21} \text{ cm}^{-3}$) and the multicomponent solid solution compound $\text{Cu}_2\text{S}_{1/3}\text{Se}_{1/3}\text{Te}_{1/3}$ ($1.50 \times 10^{21} \text{ cm}^{-3}$) are almost the same, but the room temperature Seebeck coefficient of $\text{Cu}_2\text{S}_{1/3}\text{Se}_{1/3}\text{Te}_{1/3}$ (130 $\mu\text{V K}^{-1}$) is obviously larger than that in Cu_{2-x}Se (40 $\mu\text{V K}^{-1}$). According to the single parabolic band model (see Figure S9, Supporting Information), the effective mass of monoclinic $\text{Cu}_2(\text{X} = \text{Te}, \text{Se}, \text{ or } \text{S})$ compounds is mostly below $2.0 m_e$, but it is greatly enhanced to above $4.5 m_e$ in the hexagonal structure. Such an enhancement means an increase in the electronic density of states, which is completely consistent with the upgrading of the material's crystal structure symmetry. Although there are other factors that affect the electronic properties of a material, it is very clear that the Seebeck coefficient is improved in multicomponent TE materials with increased entropy based on our data.

According to our elastic model, high-throughput predictions have been made regarding the discovery of multicomponent thermoelectric material systems, including $(\text{Cu}/\text{Ag})(\text{In}/\text{Ga})\text{Te}_2$, $\text{Cu}_2(\text{S}/\text{Se}/\text{Te})$, and $(\text{Mn}/\text{Ge}/\text{Sn}/\text{Pb})\text{Te}$. Good consistency between calculations and experiment reveals that the model presented here is reliable and effective for the screening, design, and realization of new multicomponent materials. We also expect this model to work for other materials, beyond thermoelectrics. The enhanced zT values up to 1.6 and 2.23 in respective $(\text{Cu}/\text{Ag})(\text{In}/\text{Ga})\text{Te}_2$ - and $\text{Cu}_2(\text{S}/\text{Se}/\text{Te})$ -based multicomponent TE materials demonstrate that the entropy is a gene-like performance indicator that has two significant effects on tuning and optimizing electronic and thermal transport properties, i.e., to lower κ_L by the presence of local mass and strain fluctuations and to improve the Seebeck coefficient by enhancing the crystal symmetry. While the magnitude of the two effects depends on the initial state of the matrix compounds, entropy engineering emerges as a very effective approach to design and realize high performance TE materials.

Supporting Information

Supporting Information is available from the Wiley Online Library or from the author.

Acknowledgements

R.L. and H.C. contributed equally to this work. This work was supported by the National Basic Research Program of China (973-program) under Project No. 2013CB632501 and 2017YFB0701600, the National Natural Science Foundation of China (NSFC) under the Nos. 51625205 and 51632005, the Key Research Program of Chinese Academy of Sciences (Grant No. KGZD-EW-T06), and Shanghai Government (Grant Nos. 15JC1400301, 16XD1403900 and 16XD1401100).

Conflict of Interest

The authors declare no conflict of interest.

Keywords

entropy, high-throughput, thermoelectrics

Received: May 15, 2017

Revised: July 16, 2017

Published online: August 18, 2017

- [1] G. J. Snyder, E. S. Toberer, *Nat. Mater.* **2008**, 7, 105.
- [2] G. S. Nolas, J. Sharp, H. J. Goldsmid, *Thermoelectrics: Basic Principles and New Materials Developments*, Springer, Berlin, Germany **2001**.
- [3] X. Shi, L. D. Chen, C. Uher, *Inter. Mater. Rev.* **2016**, 61, 379.
- [4] S. Curtarolo, G. L. W. Hart, M. B. Nardelli, N. Mingo, S. Sanvito, O. Levy, *Nat. Mater.* **2013**, 12, 191.
- [5] J. Yan, P. Gorai, B. Ortiz, S. Miller, S. A. Barnett, T. Mason, V. Stevanovic, E. S. Toberer, *Energy Environ. Sci.* **2015**, 8, 983.
- [6] D. T. Morelli, V. Jovovic, J. P. Heremans, *Phys. Rev. Lett.* **2008**, 101, 035901.
- [7] H. L. Liu, X. Shi, F. F. Xu, L. L. Zhang, W. Q. Zhang, L. D. Chen, Q. Li, C. Uher, T. Day, G. J. Snyder, *Nat. Mater.* **2012**, 11, 422.
- [8] K. Biswas, J. Q. He, I. D. Blum, C. I. Wu, T. P. Hogan, D. N. Seidman, V. P. Dravid, M. G. Kanatzidis, *Nature* **2012**, 489, 414.
- [9] Y. Z. Pei, X. Y. Shi, A. LaLonde, H. Wang, L. D. Chen, G. J. Snyder, *Nature* **2011**, 473, 66.
- [10] S. A. Yamini, H. Wang, Z. M. Gibbs, Y. Z. Pei, S. X. Dou, G. J. Snyder, *Phys. Chem. Chem. Phys.* **2014**, 16, 1835.
- [11] R. J. Korkosz, T. C. Chasapis, S. H. Lo, J. W. Doak, Y. J. Kim, C. I. Wu, E. Hatzikraniotis, T. P. Hogan, D. N. Seidman, C. Wolverton, V. P. Dravid, M. G. Kanatzidis, *J. Am. Chem. Soc.* **2014**, 136, 3225.
- [12] L. D. Zhao, V. P. Dravid, M. G. Kanatzidis, *Energy Environ. Sci.* **2014**, 7, 251.
- [13] Q. Shen, L. Chen, T. Goto, T. Hirai, J. Yang, G. P. Meisner, C. Uher, *Appl. Phys. Lett.* **2001**, 79, 4165.
- [14] C. Yu, T. J. Zhu, R. Z. Shi, Y. Zhang, X. B. Zhao, J. He, *Acta Mater.* **2009**, 57, 2757.
- [15] H. J. Goldsmid, *J. Appl. Phys.* **1961**, 32, 2198.
- [16] J. Jiang, L. Chen, S. Bai, Q. Yao, Q. Wang, *J. Cryst. Growth* **2005**, 277, 258.
- [17] R. E. Reed-Hill, R. Abbaschian, in *Physical Metallurgy Principles*, 3rd ed., (Eds: R. Abbaschian, R. E. Reed-Hill), PWS Publishing Company, Boston, MA **1994**, p. 272.
- [18] R. A. Swalin, in *Thermodynamics of Solids*, 2nd ed. (Eds: E. Burke, B. Chalmers, J. A. Krumhansl), Wiley, New York, NY **1991**, p. 21.
- [19] J. W. Yeh, S. K. Chen, S. J. Lin, J. Y. Gan, T. S. Chin, T. T. Shun, C. H. Tsau, S. Y. Chang, *Adv. Eng. Mater.* **2004**, 6, 299.
- [20] C. M. Rost, E. Sachet, T. Borman, A. Moballeghe, E. C. Dickey, D. Hou, J. L. Jones, S. Curtarolo, J. P. Maria, *Nat. Commun.* **2015**, 6, 8485.
- [21] S. Sakurada, N. Shutoh, *Appl. Phys. Lett.* **2005**, 86, 082105.
- [22] J. Yang, G. P. Meisner, L. Chen, *Appl. Phys. Lett.* **2004**, 85, 1140.
- [23] G. P. Meisner, D. T. Morelli, S. Hu, J. Yang, C. Uher, *Phys. Rev. Lett.* **1998**, 80, 3551.
- [24] T. Plirdpring, K. Kurosaki, A. Kosuga, T. Day, S. Firdosy, V. Ravi, G. J. Snyder, *Adv. Mater.* **2012**, 24, 3622.
- [25] F. Gascoin, S. Ottensmahn, D. Stark, S. Haile, G. Snyder, *Adv. Funct. Mater.* **2005**, 15, 1860.
- [26] W. Liu, X. J. Tan, K. Yin, H. J. Liu, X. F. Tang, J. Shi, Q. J. Zhang, C. Uher, *Phys. Rev. Lett.* **2012**, 108, 166601.

- [27] C. S. T. Dasgupta, R. Hassdorf, A. J. Zhou, L. Boettcher, E. Mueller, *Phys. Rev. B* **2011**, 83, 235207.
- [28] J. Mao, H. S. Kim, J. Shuai, Z. Liu, R. He, U. Saparamadu, F. Tian, W. Liu, Z. Ren, *Acta Mater.* **2016**, 103, 633.
- [29] W. S. Liu, K. C. Lukas, K. McEnaney, S. Lee, Q. Zhang, C. P. Opeil, G. Chen, Z. F. Ren, *Energy Environ. Sci.* **2013**, 6, 552.
- [30] A. Navrotsky, O. J. Kleppa, *J. Inorg. Nucl. Chem.* **1967**, 29, 2701.
- [31] J. K. Lee, H. J. Youn, K. S. Hong, *J. Mater. Res.* **1999**, 14, 83.
- [32] M. Posfai, P. R. Buseck, *Am. Mineral.* **1994**, 79, 308.
- [33] M. D. Gulay, O. Strok, A. Pietraszko, *Chem. Met. Alloys* **2011**, 4, 200.

ADVANCED MATERIALS

Supporting Information

for *Adv. Mater.*, DOI: 10.1002/adma.201702712

Entropy as a Gene-Like Performance Indicator Promoting
Thermoelectric Materials

*Ruiheng Liu, Hongyi Chen, Kunpeng Zhao, Yuting Qin, Binbin
Jiang, Tiansong Zhang, Gang Sha, Xun Shi,* Ctirad Uher,
Wenqing Zhang,* and Lidong Chen**

Supporting Information

Entropy as a gene-like performance indicator promoting thermoelectric materials

Ruiheng Liu†, Hongyi Chen†, Kunpeng Zhao, Yuting Qin, Binbin Jiang, Tiansong Zhang, Gang Sha, Xun Shi*, Ctirad Uher, Wenqing Zhang*, Lidong Chen*

Experimental Section

Cu shot (99.999%, Alfa Aesar), Ag shot (99.999%, Alfa Aesar), S pieces (99.9999%, Alfa Aesar), Se shot (99.999%, Alfa Aesar), Ge pieces (99.999%, Alfa Aesar), Ga shot (99.9999%, Alfa Aesar), Mn, Sn, and Pb shots (99.999%, Alfa Aesar), Te shot (99.999%, Alfa Aesar). For $\text{Cu}_{2-z}\text{Ag}_z\text{S}_{1-x-y}\text{Se}_x\text{Te}_y$, the sealed tubes were slowly cooled to 650 °C from 1100 °C at a rate of 10 °C/h and then kept at 650 °C for 8 days. The obtained ingots were crushed into fine powders and followed by Spark Plasma Sintering (Sumitomo SPS 2040) under a pressure of 60 MPa at 600 °C for 20 min. For $\text{Cu}_{1-y}\text{Ag}_y\text{In}_{1-x}\text{Ga}_x\text{Te}_2$, the silica tubes were quenched into ice cold water from 1100 °C and then annealed at 650 °C for 5 days. The obtained ingots were crushed into fine powders followed by hot press sintering (MRF Inc., USA) under a pressure of 65 MPa at 650 °C for 30 min. For $\text{Mn}_x\text{Ge}_y\text{Sn}_z\text{Pb}_{1-x-y-z}\text{Te}$, the silica tubes were slowly cooled to 550 °C at a rate of 10 °C/h from 1000 °C and kept at 550 °C for 3 days. The obtained ingots were crushed into fine powders and followed by hot press sintering (MRF Inc., USA) under a pressure of 65 MPa at 550 °C for 30 min. For $(\text{Cu}_{1-y}\text{Ag}_y)_8\text{Ge}(\text{Se}_{1-x}\text{Te}_x)_6$, the silica tubes were quenched into ice cold water from 1100 °C and then annealed at 600 °C for 5 days. The obtained ingots were crushed into fine powders and followed by Spark Plasma Sintering (Sumitomo SPS 2040) under a pressure of 60 MPa at 550 °C for 20 min.

X-ray diffraction (XRD) analysis (Cu $K\alpha$, D8 ADVANCE, Bruker Co.Ltd) was employed to examine phase purity and crystal structures. Phase composition analysis at the micrometer scale was carried out by Electron Probe Microanalysis (EPMA, ZEISS Supra

55). APT was performed at 20 K in a CAMECA instrument (LEAP 4000X Si) by applying ultraviolet laser pulsing with a wavelength of 355 nm, an energy of 10 pJ, a pulse repetition rate of 200 kHz, and a target ion collection rate of 5%. We used CAMECA IVAS 3.6.8 software to analyze the data. Samples in the form of sharp needles for APT analysis were prepared by a focused ion beam lift-off methodology (Zeiss Augruga FIB/SEM) by using Ga ion beam milling. High-temperature Seebeck coefficient (α) and electrical conductivity (σ) were measured using a ZEM-3 instrument (ULVAC Co. Ltd.) under a sealed chamber with a small amount of helium gas. The thermal diffusivity (λ) and heat capacity (C_P) from 300 K to 1000 K were measured using the laser flash method (Netzsch, LFA427) and differential scanning calorimetry (Netzsch DSC 404F3), respectively. The density (d) was measured using the Archimedes method. The thermal conductivity was calculated from $\kappa = \lambda \times C_P \times d$. Room temperature Hall coefficient (R_H) measurements were performed using Quantum Design PPMS by sweeping the magnetic field up to 3 T in both positive and negative directions. The hole concentration (p) is calculated from $p = 1/qR_H$, where q is the elementary charge.

For a binary solution reaction



the change in enthalpy $\Delta H_{A_{1-x}A'_xB}$ is

$$\Delta H_{A_{1-x}A'_xB} = H_{A_{1-x}A'_xB} - (1-x)H_{AB} - xH_{A'B} = x \int_1^x \Delta H_{cell} \cdot \frac{N_A}{Z} dt + (1-x) \int_0^x \Delta H_{cell} \cdot \frac{N_A}{Z} dt, \quad S2$$

where N_A is the Avogadro's number, and $\Delta H_{cell}(t)$ is the enthalpy change due to one $A'B$ unit cell replacing one AB unit cell in $A_{1-t}A'_tB$. $\Delta H_{cell}(t)$ has two components, the internal strain energy $\Delta H_{cell}^s(t)$ caused by the atomic size mismatch and the internal ionic field energy $\Delta H_{cell}^c(t)$ caused by electron cloud redistribution.

Assuming $A_{1-t}A'_tB$ is an elastic continuous sphere with a vacancy of one unit cell, the internal strain energies by inserting $A'B$ ($\Delta H_{A'B}^s(t)$) or AB ($\Delta H_{AB}^s(t)$) unit cells into the vacancy are calculated by using the elastic deformation equation^[1,2]

$$\Delta H_{A'B}^s(t) = \int_0^\infty \frac{1}{2} \vec{\epsilon} \vec{\delta} 4\pi r^2 dr = 8\pi G_{AA'} R_{AA'}^3 \chi_{A'}^2 c_{A'}, \quad S3$$

where $\chi_{A'} = \frac{R_{A'} - R_{AA'}}{R_{AA'}}$, $c_{A'} = \frac{3K_{A'}}{4G_{AA'} + 3K_{A'}}$, $K_{A'}$ is the bulk modulus of $A'B$, $R_{AA'}(t)$ and $G_{AA'}(t)$ are the circumradius and shear modulus of the matrix $A_{1-t}A'_tB$, respectively, which can be regarded as the linear combination of AB and $A'B$. Assuming there are tN $A'B$ unit cells dispersed in a spherical matrix with a cut-off radius \hat{R} , by adding the extra increased internal energy by the first-order effect of surface tension, $\Delta H_{A'B}^s(t)$ becomes^[3,4]

$$\Delta H_{A'B}^s(t) = 8\pi G_{AA'} R_{AA'}^3 \chi_{A'}^2 c_{A'} (1 - 2t). \quad S4$$

$\Delta H_{AB}^s(t)$ is obtained by the same approach. Then,

$$\Delta H_{cell}^s(t) = \Delta H_{A'B}^s(t) - \Delta H_{AB}^s(t) = 8\pi G_{AA'} R_{AA'}^3 \chi_{A'}^2 c_{A'} (1 - 2t) - 8\pi G_{AA'} R_{AA'}^3 \chi_A^2 c_A (2t - 1), \quad S5$$

The total increased internal strain energy ($\Delta H_S(x)$) is

$$\begin{aligned} \Delta H_S(x) &= x \int_1^x \frac{\Delta H_{cell}^s(t)}{Z} \cdot N_A dt + (1 - x) \int_0^x \frac{\Delta H_{cell}^s(t)}{Z} \cdot N_A dt \\ &\approx 8\pi \frac{N_A}{Z} G_A R_A (R_A - R_{A'})^2 \frac{3K_{A'}}{4G_A + 3K_{A'}} f_0 - 8\pi \frac{N_A}{Z} G_{A'} R_{A'} (R_A - R_{A'})^2 \frac{3K_A}{4G_{A'} + 3K_A} f_1, \end{aligned} \quad S6$$

where $f_0 = x \int_1^x (1 - t)^2 (2t - 1) dt + (1 - x) \int_0^x (1 - t)^2 (2t - 1) dt$, and $f_1 = x \int_1^x t^2 (1 - 2t) dt + (1 - x) \int_0^x t^2 (1 - 2t) dt$.

When $x = 0.5$, ΔH_S achieves its maximum value, and then $f_0 = -f_1 \approx 0.09375$. Furthermore, in semiconductors, G/K is about 0.5^[5], and $\Delta H_S(x)$ is then well-fitted by the 2nd-degree Taylor polynomial at $x = 0.5$,

$$\Delta H_S(x) \approx MN_A \cdot [\bar{G} \bar{R}^* (\Delta R^*)^2 / Z] \cdot (1 - x)x = MN_A \cdot \delta \cdot (1 - x)x, \quad S7$$

where δ is the solubility parameter (defined by $\delta = \bar{G} \bar{R}^* (\Delta R^*)^2 / Z$), R^* is the effective lattice

constant (defined by $R^* = \sqrt{\frac{a^2 + b^2 + c^2}{3}}$ for an orthorhombic structure and $\sqrt{\frac{(2a)^2 + c^2}{3}}$ for a

hexagonal structure, where a , b and c are the parameters of a unit cell, or the parameters of a supercell that is built close to a sphere), \bar{G} and \bar{R}^* are the average shear modulus and the effective lattice constant of AB and $A'B$, ΔR^* is the difference in effective lattice constants

between AB and $A'B$ ($\Delta R^* = |R_{AB}^* - R_{A'B}^*|$), $M = \frac{72\sqrt{3}\pi \times 0.09375}{4G/K + 3} \approx 7.34$.

A ternary solution $(A_{1-x}A'_x)_{1-y}A''_yB$ can be divided into three binary solutions

$$(1 - y)AB + (1 - y)A''B \rightarrow A_{1-y}A''_yB, \quad S8-1$$

$$(1 - y)A'B + (1 - y)A''B \rightarrow A'_{1-y}A''_yB, \quad S8-2$$

$$(1 - x)A_{1-y}A''_yB + xA'_{1-y}A''_yB \rightarrow (A_{1-x}A'_x)_{1-y}A''_yB, \quad S8-3$$

The change in the internal strain energy of the first two binary solutions $\Delta H_1(y)$, $\Delta H_2(y)$ can be calculated according to Equation S7. For the third quasi-binary solution, $\Delta H_3(x, y)$ is

$$\Delta H_3(x, y) \approx 8\pi \frac{N_A}{Z} G'_A R'_A (R'_A - R'_{A'})^2 \frac{3K'_{A'}}{4G'_A + 3K'_{A'}} f_0 - 8\pi \frac{N_A}{Z} G'_{A'} R'_{A'} (R'_A - R'_{A'})^2 \frac{3K'_A}{4G'_{A'} + 3K'_A} f_1, \quad S9$$

where $R'_A, R'_{A'}, R'_{AA'}, K'_A, K'_{A'}, G'_A, G'_{A'}$, have the same definitions as those in binary systems. However, Equation S9 neglects the internal stress and strain caused by the first-order effect of surface tension of the $A''B$ unit cell, which has to be considered and added. Then, f_0 and f_1 in Equation S9 are modified as

$$\begin{aligned} \hat{f}_0 &= x \int_1^x (1-t)^2 \left(2t - 1 - 2 \frac{R_{A''} - R'_{AA'}}{R'_A - R'_{AA'}} y \right) dt + (1-x) \int_0^x (1-t)^2 \left(2t - 1 - 2 \frac{R_{A''} - R'_{AA'}}{R'_A - R'_{AA'}} y \right) dt \quad \text{and} \\ \hat{f}_1 &= x \int_1^x t^2 \left(1 - 2t - 2 \frac{R_{A''} - R'_{AA'}}{R'_A - R'_{AA'}} y \right) dt + (1-x) \int_0^x t^2 \left(1 - 2t - 2 \frac{R_{A''} - R'_{AA'}}{R'_A - R'_{AA'}} y \right) dt. \end{aligned}$$

To simplify $\Delta H_3(x, y)$, it can be written as a product of two terms

$$\Delta H_3(x, y) \approx \Delta H_3(x, 0) \cdot f(y, \frac{R_{A''}}{R_{AA'}}). \quad S10$$

where $\Delta H_3(x, 0)$ is the internal strain energy for a binary solution $A_{1-x}A'_xB$, and $f(y, \frac{R_{A''}}{R_{AA'}})$ is a function representing the effect of an extra component $A''B$. As shown in Figure S2, the $f(y, \frac{R_{A''}}{R_{AA'}})$ can be well fit by $(1-y)^{3.5}$ when $\frac{R_{A''}}{R_{AA'}}$ varies from 80% ~ 120%. Thus,

$$\Delta H_3(x, y) \approx MN_A \cdot \delta_{AA'} \cdot (1-x)x \cdot (1-y)^{3.5}, \quad S11$$

where $\delta_{AA'}$ is the solubility parameter of a binary solution $A_{1-x}A'_xB$.

Consequently, the calculated total internal strain energy of the ternary solution in Equation S8 is

$$\Delta H_{\text{total}} = x\Delta H_1(y) + (1-x)\Delta H_2(y) + \Delta H_3(x, y), \quad S12$$

Considering all the different solution routes, the average ΔH_{total} for achieving an equimolar ternary solution is

$$\Delta \bar{H}_{\text{total}} = MN_A \cdot \bar{\delta} \cdot \left[\sum_{i=2}^3 \left(1 - \frac{1}{i} \right) \frac{1}{i} \cdot \left(\frac{i}{3} \right)^{3.5} \right], \quad S13$$

where $\bar{\delta}$ is the average δ value of all separate binary solutions.

Using the same approach, for a multi-component material $(A_{1-x}A'_x)_{1-y_1-y_2...}A''_{y_1}A'''_{y_2}...B$, $\Delta H_5(x, y_1, y_2 \dots)$ we write

$$\Delta H_5(x, y_1, y_2 \dots) \approx MN_A \cdot \delta_{AA'} \cdot (1-x)x \cdot (1-y_{\text{total}})^{3.5}, \quad S14$$

where $y_{\text{total}} = y_1 + y_2 + \dots$. For equimolar multi-component solutions, $\Delta \bar{H}_{\text{total}}$ is given by

$$\Delta \bar{H}_{\text{total}} = MN_A \cdot \bar{\delta} \cdot \left[\sum_{i=2}^n \left(1 - \frac{1}{i} \right) \frac{1}{i} \cdot \left(\frac{i}{n} \right)^{3.5} \right]. \quad S15$$

For the change in the internal ionic field energy $\Delta H_{cell}^c(t)$, the effective charge (Q) of A (or A') in AB (or $A'B$) is estimated and calculated based on the developed Pauling electronegativity^[6]. For $A_{1-t}A'_tB$, the average effective charge of A (A') atomic positions can be assumed to be a linear combination of Q_A and $Q_{A'}$. Then, according to the Born–Landé equation^[7], $\Delta H_{cell}^c(t)$ is

$$\Delta H_{cell}^c(t) = -\frac{M_A \cdot Q_{AA'} \cdot (Q_A - Q_{A'})}{4\pi\epsilon_0 R_{AA'}} - \frac{M_B \cdot Q_B \cdot (Q_A - Q_{A'})}{4\pi\epsilon_0 R_{AA'}}, \quad S16$$

where ϵ_0 is the vacuum permittivity, and M_A and M_D are the Madelung constants for atom A (A') and B . $\Delta H_c(x)$ then becomes

$$\Delta H_c(x) = x \int_1^x -\Delta H_{cell}^c(t) \cdot N_A dt + (1-x) \int_0^x -\Delta H_{cell}^c(t) \cdot N_A dt. \quad S17$$

The calculated ΔH_S and ΔH_c for several TE materials are listed in Table S1.

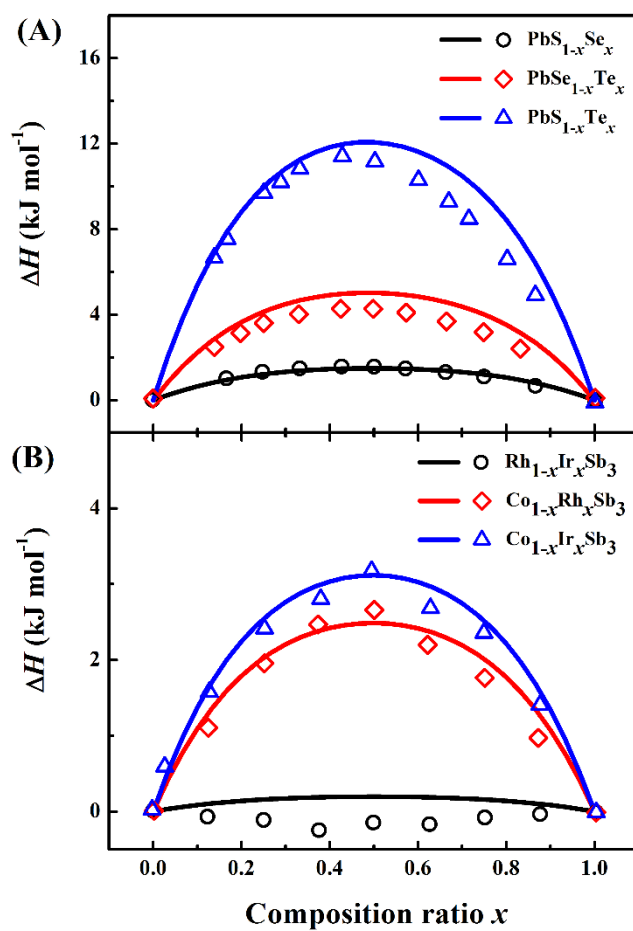
Figures S1 to S9.

Figure S1. Calculated changes in enthalpy (ΔH) based on Equation S6 for several two-component TE materials. The lines are calculated according to our model. The dots are calculated by *ab initio* calculations taken from Supporting Ref. 8 and 9.

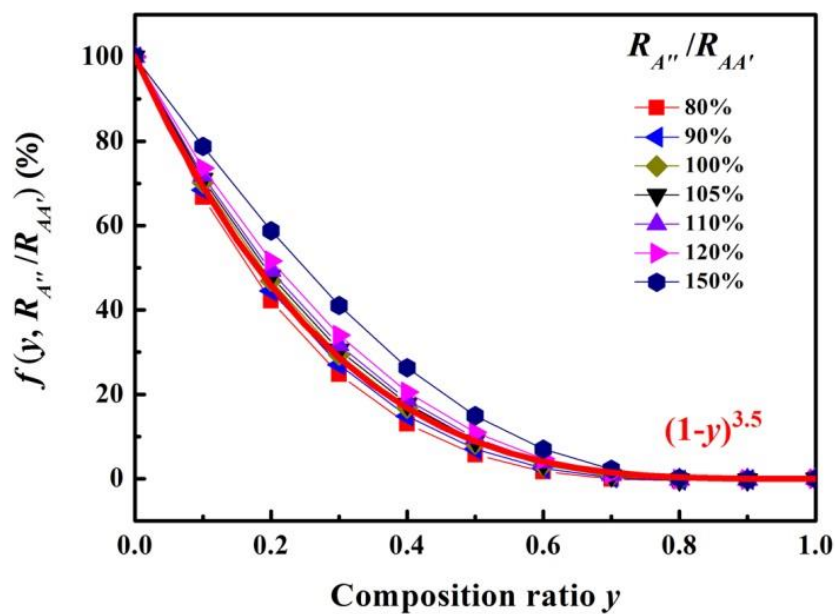


Figure S2. Function $f(y, \frac{R_{A''}}{R_{AA'}})$ depending on y and $\frac{R_{A''}}{R_{AA'}}$. Curves marked with symbols are calculated according to Equation S9, and the red curve is the fitting result represented by $(1-y)^{3.5}$.

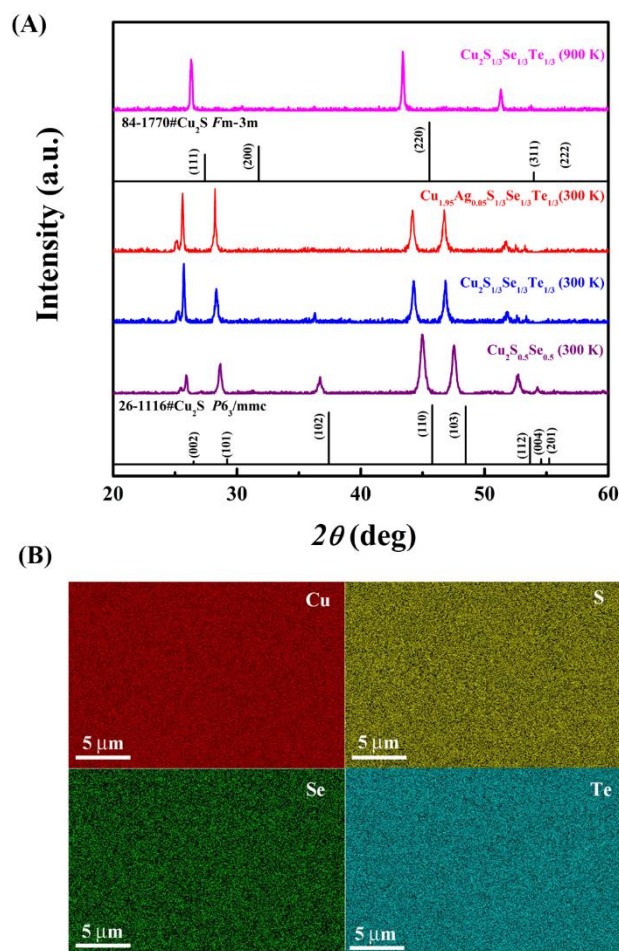


Figure S3. (A) Powder X-ray diffraction patterns of $\text{Cu}_2\text{S}_{0.5}\text{Se}_{0.5}$, $\text{Cu}_2\text{S}_{1/3}\text{Se}_{1/3}\text{Te}_{1/3}$, and $\text{Cu}_{1.95}\text{Ag}_{0.05}\text{S}_{1/3}\text{Se}_{1/3}\text{Te}_{1/3}$. They exhibit a hexagonal structure with the space group of $P6_3/\text{mmc}$ at 300 K. The uppermost trace shows a cubic structure of $\text{Cu}_2\text{S}_{1/3}\text{Se}_{1/3}\text{Te}_{1/3}$ with the space group of $Fm-3m$ at 900 K. (B) Elemental maps of $\text{Cu}_2\text{S}_{1/3}\text{Se}_{1/3}\text{Te}_{1/3}$ obtained by Electron Probe Microanalysis (EPMA).

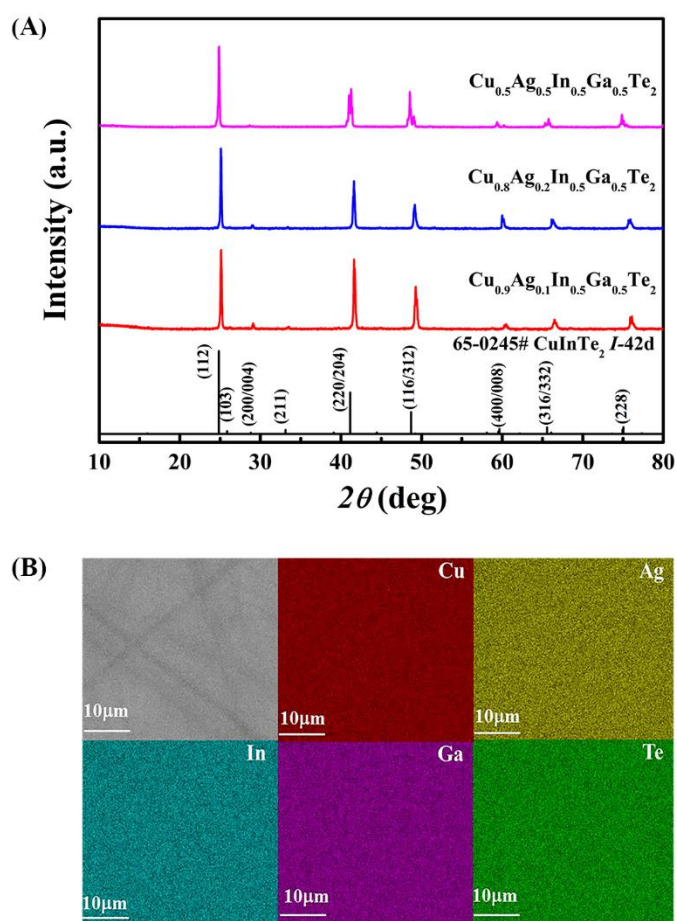


Figure S4. (A) Powder X-ray diffraction patterns of a series of $(\text{Cu}/\text{Ag})(\text{In}/\text{Ga})\text{Te}_2$ -based multi-component TE materials. (B) Elemental maps of $\text{Cu}_{0.5}\text{Ag}_{0.5}\text{In}_{0.5}\text{Ga}_{0.5}\text{Te}_2$ obtained by Electron Probe Microanalysis (EPMA).

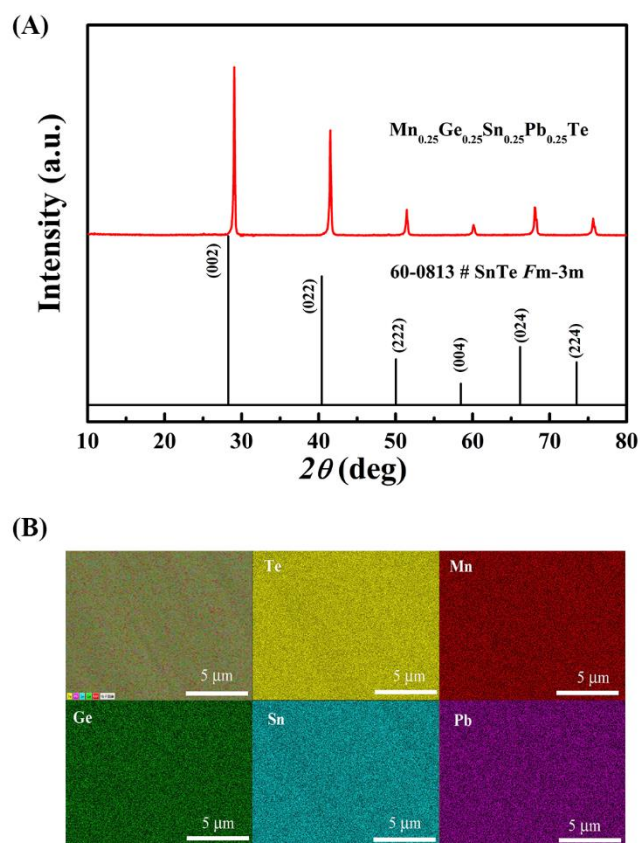


Figure S5. (A) Powder X-ray diffraction pattern of $\text{Mn}_{0.25}\text{Ge}_{0.25}\text{Sn}_{0.25}\text{Pb}_{0.25}\text{Te}$. (B) Elemental maps of $\text{Mn}_{0.25}\text{Ge}_{0.25}\text{Sn}_{0.25}\text{Pb}_{0.25}\text{Te}$ obtained by Electron Probe Microanalysis (EPMA).

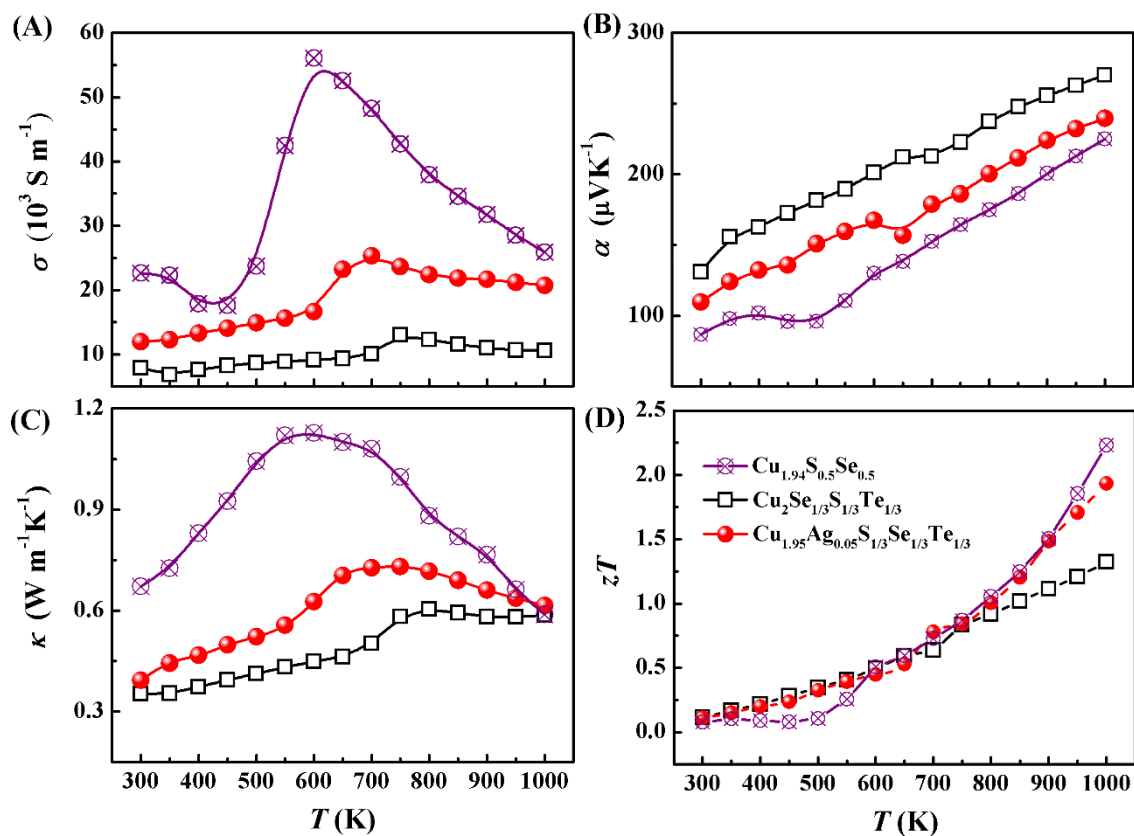


Figure S6. Temperature dependence of the electrical conductivity (A), Seebeck coefficient (B), thermal conductivity (C) and the thermoelectric figure of merit (zT) (D) for $\text{Cu}_2(\text{S}/\text{Se}/\text{Te})$ -based multi-component TE materials.

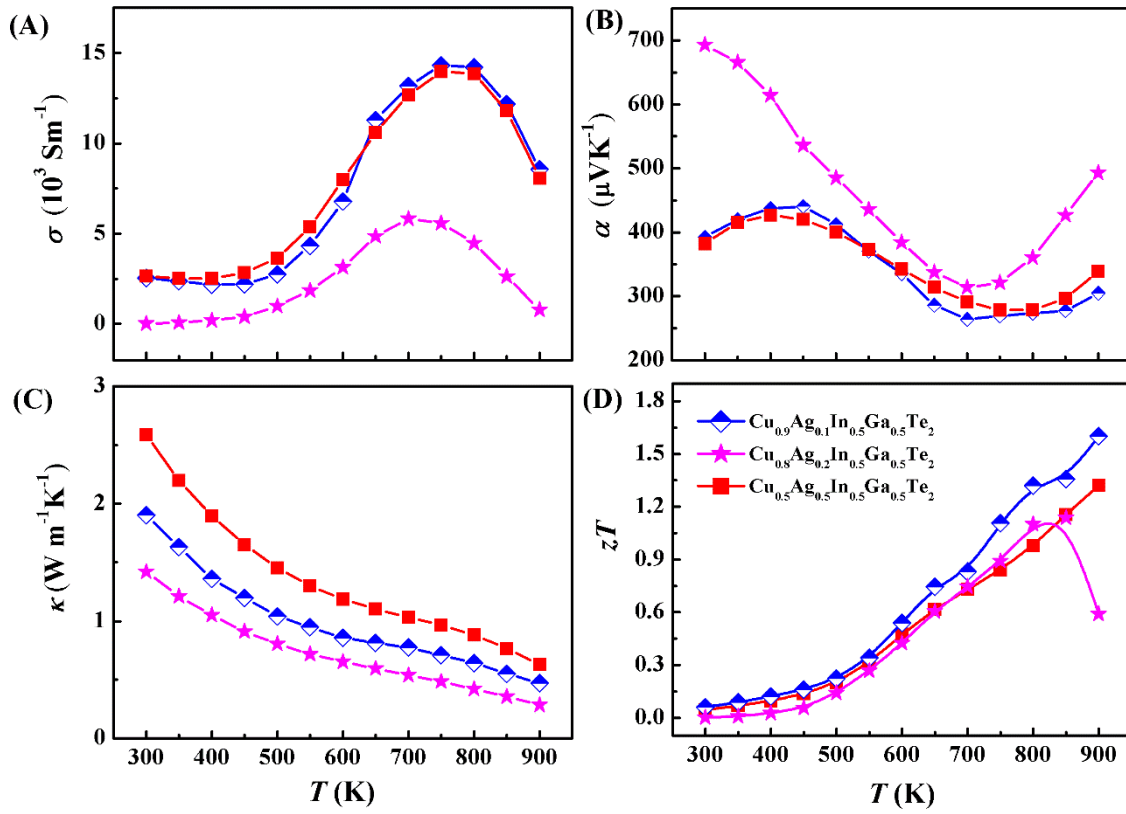


Figure S7. Temperature dependence of the electrical conductivity (A), Seebeck coefficient (B), thermal conductivity (C) and the figure of merit (zT) (D) for $(\text{Cu/Ag})(\text{In/Ga})\text{Te}_2$ -based multi-component TE materials.

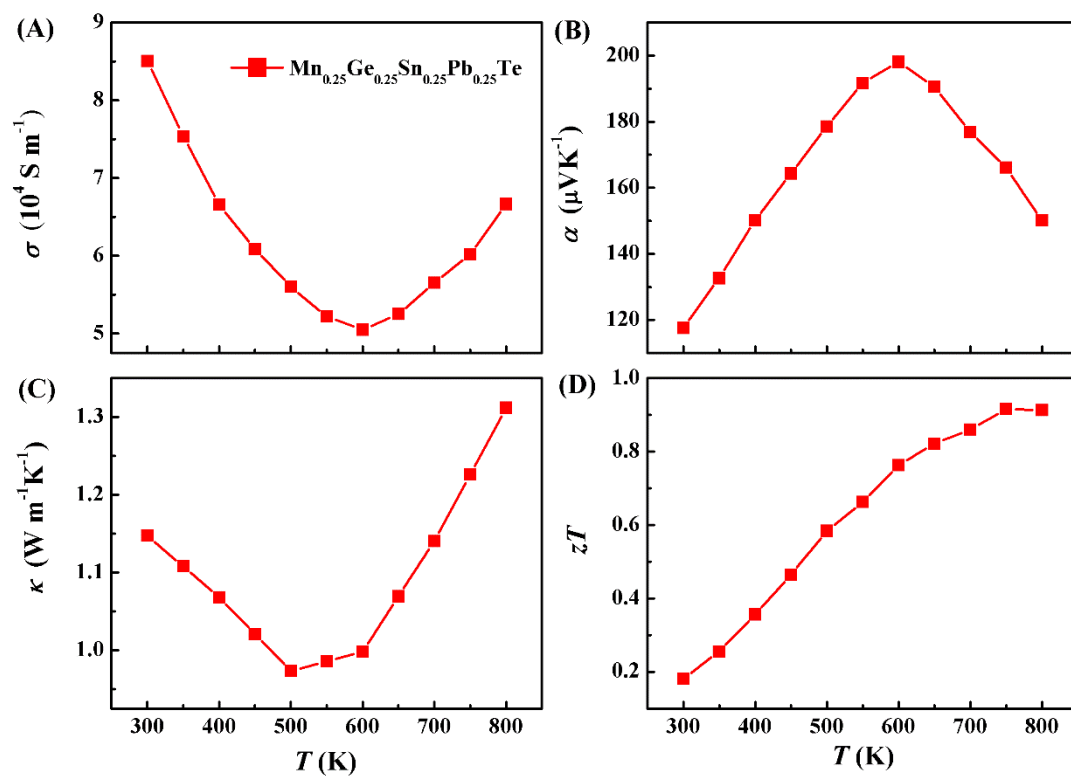


Figure S8. Temperature dependence of the electrical conductivity (A), Seebeck coefficient (B), thermal conductivity (C) and the figure of merit (zT) (D) for $\text{Mn}_{0.25}\text{Ge}_{0.25}\text{Sn}_{0.25}\text{Pb}_{0.25}\text{Te}$ multi-component TE materials.

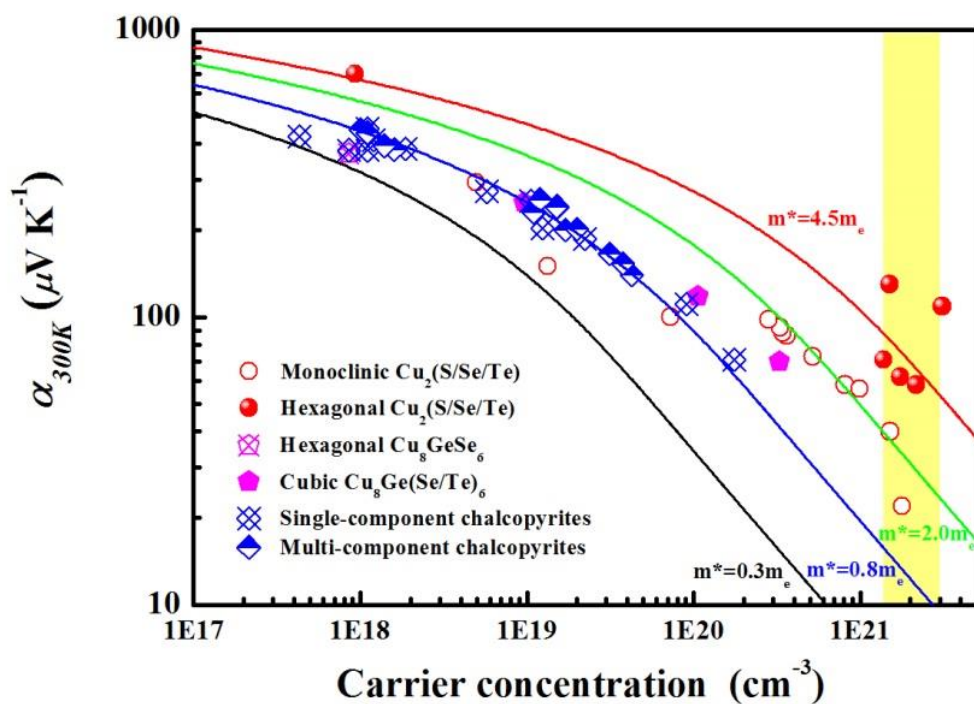


Figure S9. Hall carrier concentration dependence of room temperature Seebeck coefficient of $\text{Cu}_2(\text{S/Se/Te})$ -, $(\text{Cu/Ag})(\text{In/Ga})\text{Te}_2$ -, and $\text{Cu}_8\text{Ge}(\text{Se/Te})_6$ -based TE materials. The effective mass is estimated from the single parabolic band model.

Tables S1 to S4.**Table S1.** Internal strain energy (ΔH_S) arising from the atomic size mismatch, fluctuation of the internal ionic field energy (ΔH_C) from electron cloud redistribution, $\Delta H_C/\Delta H_S$, and the formation enthalpy (ΔH) for various binary TE solutions with equal atomic-ratio components.

Systems	ΔH_C [J mol ⁻¹]	ΔH_C [$k_B T$ /f.u.]	ΔH_S [J mol ⁻¹]	$\Delta H_C/\Delta H_S$	ΔH [J/mol]
PbSe-PbTe	316.7	0.13	5025.8	6.30%	5342.5
PbS-PbTe	40.3	0.02	12069.6	0.33%	12109.9
PbS-PbSe	-38.9	-0.02	1499.1	-2.59%	1460.2
CoSb ₃ -IrSb ₃	440.5	0.18	3116.8	14.13%	3557.3
CoSb ₃ -RhSb ₃	916.5	0.37	2487.0	36.85%	3403.5
CuInTe ₂ -AgInTe ₂	13.8	<0.01	276.9	4.98%	290.7

Table S2. Space group, number of components (n), average shear modulus (\bar{G}), average effective lattice constant (\bar{R}^*), and parameter $\bar{\delta}$ for various systems of multi-component TE materials.

NO.	Systems	Space group	n	\bar{G} [GPa]	\bar{R}^* [Å]	$\bar{\delta}$ [GPa·Å ³]
1	TiCoSb-ZrCoSb-HfCoSb	$Fm-3m$	3	76	6.01	1.85
2	CoSb ₃ -RhSb ₃ -IrSb ₃	$Im-3$	3	63	9.18	2.14
3	Cu ₂ S-Cu ₂ Se-Cu ₂ Te	(LT) $P2_1/c$, $C2/c$; (MT) $P6_3/mmc$; (HT) $Fm-3m$	3	26	5.91	2.39
4	ZnTe-CdTe-HgTe	$F-43m$	3	16	6.35	2.40
5	TiNiSn-ZrNiSn-HfNiSn	$F-43m$	3	90	6.04	2.45
6	CuGaTe ₂ -CuInTe ₂ -AgGaTe ₂ -AgInTe ₂	$I-42d$	4	22	8.71	3.12
7	MnTe-GeTe-SnTe-PbTe	$Fm-3m$	4	19	6.18	3.36
8	PbS-PbSe-PbTe	$Fm-3m$	3	27	6.19	4.57
9	AlSb-GaSb-InSb	$F-43m$	3	53	6.25	7.01

Table S3. Seebeck coefficient (α), electrical conductivity (σ), thermal conductivity (κ), carrier concentration (p) at 300 K, and the maximum TE figure of merit at corresponded temperatures ($(zT)_{max}$) of various single component and multi-component TE materials.

Compositions	α [$\mu\text{V K}^{-1}$]	σ [S m^{-1}]	κ [$\text{W m}^{-1}\text{K}^{-1}$]	P [cm^{-3}]	$(zT)_{max}$
$\text{Cu}_{1.92}\text{S}^{[10]}$	40	4.10×10^4	1.06	2.50×10^{21}	0.57
$\text{Cu}_{1.9}\text{Se}$	40	3.48×10^5	2.16	1.51×10^{21}	0.43
$\text{Cu}_2\text{Te}^{11}$	25	4.10×10^5	2.08	1.78×10^{21}	0.56
$\text{Cu}_2\text{Se}_{0.8}\text{Te}_{0.2}$	44	1.32×10^5	1.37	1.10×10^{21}	0.80
$\text{Cu}_2\text{Se}_{0.5}\text{Te}_{0.5}$	40	1.20×10^5	1.03	1.12×10^{21}	1.11
$\text{Cu}_2\text{S}_{0.50}\text{Te}_{0.50}^{[12]}$	58	3.13×10^4	0.52	2.17×10^{21}	2.10
$\text{Cu}_2\text{S}_{0.52}\text{Te}_{0.48}^{[12]}$	62	2.77×10^4	0.48	1.74×10^{21}	1.83
$\text{Cu}_2\text{S}_{0.54}\text{Te}_{0.46}^{[12]}$	71	1.92×10^4	0.41	1.37×10^{21}	1.70
$\text{Cu}_{1.94}\text{S}_{0.5}\text{Se}_{0.5}$	87	2.27×10^4	0.67	1.34×10^{21}	2.23
$\text{Cu}_2\text{S}_{1/3}\text{Se}_{1/3}\text{Te}_{1/3}$	130	7.87×10^3	0.35	1.50×10^{21}	1.32
$\text{Cu}_{1.95}\text{Ag}_{0.05}\text{S}_{1/3}\text{Se}_{1/3}\text{Te}_{1/3}$	109	1.19×10^4	0.39	3.01×10^{21}	1.92
CuInTe_2^{13}	204	9.70×10^3	6.03	1.24×10^{19}	1.02
$\text{Cu}_{0.99}\text{GaTe}_2^{[14]}$	263	1.59×10^4	7.80	1.22×10^{19}	0.70
$\text{Cu}_{0.99}\text{In}_{0.5}\text{Ga}_{0.5}\text{Te}_2^{[14]}$	202	2.54×10^4	3.50	1.59×10^{19}	0.82
$\text{Cu}_{0.88}\text{Ag}_{0.1}\text{InTe}_2^{[15]}$	201	1.35×10^4	2.84	1.70×10^{19}	1.09
$\text{Cu}_{0.75}\text{Ag}_{0.2}\text{InTe}_2^{[15]}$	231	7.10×10^3	1.84	1.11×10^{19}	1.24
$\text{Cu}_{0.88}\text{Ag}_{0.1}\text{InTe}_2^{[15]}$	211	1.42×10^4	2.90	2.00×10^{19}	0.68
$\text{Cu}_{0.75}\text{Ag}_{0.2}\text{InTe}_2^{[15]}$	242	8.20×10^3	1.95	1.52×10^{19}	0.77
$\text{Cu}_{0.9}\text{Ag}_{0.1}\text{In}_{0.5}\text{Ga}_{0.5}\text{Te}_2$	382	2.63×10^3	2.58	1.75×10^{18}	1.32
$\text{Cu}_{0.8}\text{Ag}_{0.2}\text{In}_{0.5}\text{Ga}_{0.5}\text{Te}_2$	392	2.55×10^3	1.90	1.90×10^{18}	1.60
$\text{Cu}_{0.5}\text{Ag}_{0.5}\text{In}_{0.5}\text{Ga}_{0.5}\text{Te}_2$	693	2.54×10^1	1.42	-	1.13
$\text{Mn}_{0.25}\text{Ge}_{0.25}\text{Sn}_{0.25}\text{Pb}_{0.25}\text{Te}$	118	4.98×10^4	1.15	-	0.91
Cu_8GeSe_6	235	3.23×10^0	0.31	8.48×10^{17}	0.54
$\text{Cu}_8\text{GeSe}_{5.7}\text{Te}_{0.3}$	284	1.52×10^2	0.29	9.56×10^{18}	0.71
$\text{Cu}_8\text{GeSe}_{5.4}\text{Te}_{0.6}$	104	1.35×10^4	0.51	1.06×10^{20}	0.89
$\text{Cu}_{7.6}\text{Ag}_{0.4}\text{GeSe}_{5.1}\text{Te}_{0.9}$	88	3.57×10^4	0.41	4.38×10^{20}	1.07

Table S4. Space group, shear modulus (G), lattice parameters (a and c), unit cell volume (V_{cell}), number of formula units (Z) in one unit cell for typical TE materials.

Compounds	Space group	G [GPa]	Lattice parameter		V_{cell} [Å ³]	Z
			a [Å]	c [Å]		
PbS	$Fm-3m$	30	5.996	-	215	4
PbSe	$Fm-3m$	27	6.140	-	231	4
PbTe	$Fm-3m$	23	6.440	-	268	4
Bi ₂ Te ₃ ^{a)}	$R-3m$	52	4.390	30.480	-	3
Sb ₂ Te ₃ ^{a)}	$R-3m$	-	4.260	30.400	-	3
Bi ₂ Se ₃ ^{a)}	$R-3m$	-	4.130	28.600	-	3
SnTe	$Fm-3m$	10	6.310	-	251	4
GeTe	$Fm-3m$	25	5.985	-	214	4
MnTe	$Fm-3m$	-	5.980	-	214	4
CoSb ₃	$Im-3$	56	9.034	-	737	8
RhSb ₃	$Im-3$	63	9.242	-	786	8
IrSb ₃	$Im-3$	70	9.253	-	792	8
CuInTe ₂	$I-42d$	19	6.194	12.416	476	4
AgInTe ₂	$I-42d$	14	6.401	12.613	515	4
CuGaTe ₂	$I-42d$	26	6.024	11.929	432	4
AgGaTe ₂	$I-42d$	28	6.296	11.990	475	4
ZnTe	$F-43m$	20	6.104	-	227	4
CdTe	$F-43m$	18.3	6.481	-	272	4
HgTe	$F-43m$	8.9	6.461	-	270	4
Cu ₂ S	(HT) $Fm-3m$ ^{b)}	17.8 ^{c)}	5.762	-	191	4
Cu ₂ Se	(HT) $Fm-3m$ ^{b)}	36.3 ^{c)}	5.871	-	202	4
Cu ₂ Te	(HT) $Fm-3m$ ^{b)}	25 ^{c)}	6.114	-	228	4
AlSb	$F-43m$	58	6.135	-	231	4
GaSb	$F-43m$	56	6.118	-	229	4
InSb	$F-43m$	46	6.487	-	273	4
TiNiSn	$Fm-3m$	76	5.921	-	208	4
ZrNiSn	$Fm-3m$	-	6.113	-	228	4
HfNiSn	$Fm-3m$	-	6.084	-	225	4
TiCoSb	$Fm-3m$	90.5	5.913	-	207	4
ZrCoSb	$Fm-3m$	-	6.068	-	223	4
HfCoSb	$Fm-3m$	-	6.040	-	220	4

SrZn ₂ Sb ₂	<i>P</i> -3m1	-	4.500	7.716	135	1
CaZn ₂ Sb ₂	<i>P</i> -3m1	-	4.441	7.464	127	1
EuZn ₂ Sb ₂	<i>P</i> -3m1	25	4.480	7.601	133	1
YbZn ₂ Sb ₂	<i>P</i> -3m1	-	4.446	7.426	127	1

^{a)} For Bi₂Te₃-based materials, a supercell with lattice parameters of ($4a^* \times 4b^* \times c^*$) is used, where a^* , b^* , and c^* are the lattice parameters of a conventional unit cell;

^{b)} The lattice parameters of high temperature cubic structure are used^[16,17];

^{c)} Shear modulus is calculated based on the reported acoustic velocity^[11,18].

Supporting References:

- [1] D. Feng, D. R. Qiu, *Physics in metals: Structure and Defects*, Beijing: Science press, **1998**, p. 172.
- [2] J. D. Eshelby, *Solid State Phys.* **1956**, 3, 79.
- [3] H. Sonomura, *J. Appl. Phys.* **1986**, 59(3), 739.
- [4] W. S. Slaughter, *The linearized theory of elasticity*, Birkhauser, Boston, **2002**, p. 193.
- [5] G. N. Greaves, A. L. Greer, R. S. Lakes, T. Rouxel, *Nat. Mater.* **2011**, 10, 823.
- [6] J. C. Phillips, *Rev. Mod. Phys.* **1970**, 42(3), 317.
- [7] I. D. Brown, *The chemical bond in inorganic chemistry: the bond valence model* (Reprint. ed.), Oxford University Press, Oxford, **2002**.
- [8] J. W. Doak, C. Wolverton, *Phys. Rev. B* **2012**, 86, 144202.
- [9] X. Shi, Z. Zhou, W. Zhang, L. D. Chen, J. Yang, C. Uher, *J. Appl. Phys.* **2007**, 101(12), 123525.
- [10] P. F. Qiu, Y. Q. Zhu, Y. T. Qin, X. Shi, L. D. Chen, *APL Mater.* **2016**, 4, 104805.
- [11] Y. He, T. S. Zhang, X. Shi, S. H. Wei, L. D. Chen, *NPG Asia Mater.* **2015**, 7, e210.
- [12] Y. He, P. Lu, X. Shi, F. F. Xu, T. S. Zhang, G. J. Snyder, C. Uher, L. D. Chen, *Adv. Mater.* **2015**, 27(24), 3639.
- [13] N. Cheng, R. H. Liu, S. Q. Bai, X. Shi, L. D. Chen, *J. Appl. Phys.* **2014**, 115, 163705.
- [14] Y. T. Qin, P. F. Qiu, R. H. Liu, Y. L. Li, F. Hao, T. S. Zhang, D. D. Ren, X. Shi, L. D. Chen, *J. Mater. Chem. A* **2016**, 4, 1277.
- [15] R. H. Liu, Y. T. Qin, N. Cheng, J. W. Zhang, X. Shi, Y. Grin, L. D. Chen, *Inorg. Chem. Front.* **2016**, 3, 1167.
- [16] M. Oliveria, R. K. McMullan, B. J. Wuensch, *Solid State Ionics* **1988**, 28, 1332.
- [17] Y. G. Asadov, S. Y. Asadova, A. Movlamverdieva, F. K. Isaev, *Inor. Mater.* **2002**, 38, 1103.
- [18] Y. He, T. Day, T. S. Zhang, X. Shi, L. D. Chen, G. J. Snyder, *Adv. Mater.* **2014**, 26(23), 3974.